



RESEARCH ARTICLE OPEN ACCESS

Glutamatergic Regulation of miRNA-Containing Intraluminal Vesicle Trafficking and Extracellular Vesicle Secretion From Cortical Neurons

Marcela Bertolio¹ | Qiyi Li¹ | Francesca E. Mowry¹ | Kathryn E. Reynolds¹  | Rashed Alananzeh¹ | Haichao Wei³ | Kyoeun Keum¹ | Rachel Jarvis¹ | Jiaqian Wu³ | Yongjie Yang^{1,2} 

¹Department of Neuroscience, Tufts University School of Medicine, Boston, Massachusetts, USA | ²Graduate School of Biomedical Sciences, Tufts University, Boston, Massachusetts, USA | ³Department of Neurosurgery, McGovern Medical School, The University of Texas Health Science Center at Houston (UTHealth), Houston, Texas, USA

Correspondence: Yongjie Yang (yongjie.yang@tufts.edu)

Received: 25 September 2024 | **Accepted:** 8 May 2025

Funding: This work was supported by NIH grants R01NS118747, R01NS125490 and R01AG078728.

Keywords: CD63 | extracellular vesicles | glutamate stimulation | intraluminal vesicles (ILVs) | microRNA

ABSTRACT

Neuronal extracellular vesicles (microvesicles and exosomes) are emerging secreted vesicular signals that play important roles in the CNS. Currently, little is known about how glutamatergic signalling affects the subcellular localisation of exosome precursor intraluminal vesicles (ILVs), microRNA (miR) packaging into ILVs and in vivo spreading of neuronal EVs. By selectively labelling ILVs and exosomes (but not plasma membrane-derived MVs) with GFP-tagged human CD63 (hCD63-GFP) in cortical neurons, we found that glutamate stimulation significantly redistributes subcellular localisation of hCD63-GFP⁺ ILVs, especially decreasing its co-localisation with multi-vesicular body (MVB) marker Rab7 while substantially promoting EV secretion. Interestingly, glutamate stimulation only modestly alters EV miR profiles based on small RNA sequencing. Subsequent in vivo cortical neuronal DREADD activation leads to significantly more widespread hCD63-GFP⁺ area in hCD63-GFP^{f/+} mice, consistently supporting the stimulatory effect of glutamatergic activation on neuronal EV secretion and spreading. Moreover, in situ localisation of hCD63-GFP⁺ ILVs and hCD63-GFP⁺ secreted exosomes from specialised HB9⁺ and DAT⁺ neurons were also illustrated in the CNS. Taken together, our results demonstrated that glutamate activity stimulates neuronal exosome secretion and spreading in vitro and in vivo, but only modestly affects miR cargo packaging in neuronal exosomes.

1 | Introduction

Extracellular vesicles (EVs, size 100–1000 nm), primarily composed of plasma membrane-shed microvesicles (MVs) and endosome-derived exosomes, are emerging to mediate important communication among heterogeneous CNS cell types (Blanchette and Rodal 2020; Budnik et al. 2016; Wan et al. 2022). Neuron-secreted EVs facilitate miRNA (miR) transfer into astrocytes or endothelial cells to subsequently up-regulate astroglial glutamate

transporter GLT1 expression or to regulate brain vascular integrity (Men et al. 2019; Morel et al. 2013; Xu et al. 2017). Brain-derived neurotrophic factor (BDNF) induces miR sorting into neuron-secreted EVs which in turn increase excitatory synapse formation in recipient hippocampal neurons (Antoniou et al. 2023). Neuronal proteins Arc and PEG10 also share homology with retrotransposon Gag that can form EVs to facilitate transfer of mRNA between neurons (Pastuzyn et al. 2018; Segel et al. 2021). In vivo transmission electron microscopy, tracing and

This is an open access article under the terms of the [Creative Commons Attribution-NonCommercial-NoDerivs](https://creativecommons.org/licenses/by-nc-nd/4.0/) License, which permits use and distribution in any medium, provided the original work is properly cited, the use is non-commercial and no modifications or adaptations are made.

© 2025 The Author(s). *Journal of Extracellular Vesicles* published by Wiley Periodicals LLC on behalf of International Society for Extracellular Vesicles.

proteomic experiments further demonstrated the involvement of EVs in mediating transfer of transneuronally transported proteins (TNTPs) from retinogeniculate inputs to excitatory lateral geniculate nucleus (LGN) neurons and further to neurons in visual cortex (Schiapparelli et al. 2022). EV signalling was also found to mediate the transfer of Wingless (Wg) from synaptic boutons to the specialised muscle region sub synaptic reticulum (SSR) in the neuromuscular junction (NMJ) of fly larva (Koles et al. 2012) and prevents accumulation of ciliary cargo in *Caenorhabditis elegans* sensory neurons (Razzauti and Laurent 2021). Additionally, neuronal EVs have been shown to associate with various disease-causing mutant proteins in both neurodegenerative disease models and human CSF and plasma fluid (Delpesch et al. 2019; Kim et al. 2022; You et al. 2023).

The understanding of the cellular regulation of EV secretion from neurons by glutamatergic neurotransmission, the predominant signalling in the CNS, is at very beginning. Early in vitro studies showed that cultured cortical neurons secrete elevated number of EVs upon KCL-induced depolarisation (Faure et al. 2006; Olivero et al. 2021) and GABAergic blockade (Lachenal et al. 2011) based on increased detection of EV protein markers. A number of other factors, ranging from disease-relevant proteins such as TDP43 and Tau to BDNF (Antonioni et al. 2023; Iguchi et al. 2016; Wang et al. 2017), also stimulate EV secretion from cultured neurons. However, the ultracentrifugation isolation and EV marker immunoblot-based quantification of secreted EVs used in early studies tend to induce EV damage and aggregation (Kim et al. 2022). These approaches are also less quantitative. In addition, although EVs with putative neuronal surface markers are commonly found in human CSF in control and disease subjects (Hill 2019), whether neuronal activity regulates in vivo neuronal EV secretion and spreading remains unexplored. Similarly, whether the packaging of miRs, a major type of cargo in EV especially exosomes, into exosome precursor ILVs is influenced by neuronal glutamatergic activity is unknown, nor are whether the compartmental and subcellular distribution of ILVs. In the current study, by selectively inducing GFP-tagged ILV and exosome marker human CD63 (hCD63-GFP) in cortical neurons, we began to address these questions. We also illustrated in situ localisation of ILVs and secreted EVs from specialised dopaminergic and motor neurons in midbrain and spinal cord respectively, and how DREADD-mediated neuronal activation affects in vivo spreading of neuronal EVs in the cortex.

2 | Materials and Methods

2.1 | Animals

Human (h) CD63-GFP^{f/f} knock-in mice were previously generated and characterised by the lab (Men et al. 2019). Wild type (C57BL/6J background, #00664), DAT-Cre congenic (#006660), HB9-Cre congenic (#006600) and Ai14-tdT^{f/f} congenic mice (#007914) were obtained from The Jackson Laboratory. Male and female mice were used in all experiments, and they were maintained on a 12-h light/dark cycle with ad libitum access to food and water. All animal care and treatment procedures were strictly carried out in accordance with the NIH Handbook for the

Care and Use of Laboratory Animals and the Guidelines for the Use of Animals in Neuroscience Research. The animal techniques utilised in this study were approved (protocol number: B2022-50) by the Tufts University's Institutional Animal Care and Use Committee (IACUC).

2.2 | Drug Administration

Clozapine-N-oxide (CNO) was reconstituted at a concentration of 10 mg/mL in DMSO and subsequently diluted in saline to a final concentration of 0.5 mg/mL as a working dosage. The mice received CNO via intraperitoneal injection (i.p.) at a dose of 0.3 mg/kg, 2 weeks following stereotaxic surgery. After injection, the mice were kept alive for 1 h to assess neuronal activation, or 3 h for ILVs/EV spreading analysis.

2.3 | Primary Neuronal Culture and Transfection

For neuronal primary cultures, cortical neurons were isolated from embryonic day 14–16 mouse brains. Cerebellum, olfactory bulbs, meninges and hippocampus were removed from each brain. Cortices were placed into 0.05% trypsin solution for 10 min in a 37°C bead bath. The enzymatic reaction was stopped by addition of neuron plating medium (NPM), composed of neurobasal medium, 2% B27 neurobasal supplement, 2 mM glutamine, 1% of 100x GlutaMAX, 1% penicillin–streptomycin and 5% EV-free fetal bovine serum. The tissue was gently dissociated by pipetting with a 1 mL micropipette and dissociated cells were filtered through a 70 µm strainer to collect the neuron cell suspension. Freshly prepared neurons were then plated on 10 cm cell culture dishes (5 × 10⁶ cells) precoated with Poly-L-Lysine (0.1 µg/mL) and laminin (50 µg/mL), or on precoated 12 mm diameter coverslips (Neuvitro Corporation) (2.5 × 10⁴ cells) placed in 24-well plates. The cultures were kept in NPM for 24 h and then the media was replaced by neuron growth media (NGM) composed of neurobasal medium, 2% B27 neurobasal supplement, 2 mM glutamine, 1% of 100x GlutaMAX and 1% penicillin–streptomycin. Neuronal cultures have typically less than 2% of glial cells based on GFAP immunostaining. To induce the expression of hCD63-GFP, AAV9-CaMKII-0.4.Cre (final concentration 1 × 10¹⁰ genome copy (gc)/mL; Addgene, #105558) was added to primary neuronal cultures at 1 day in vitro (DIV). Primary neurons transfection on precoated coverslips with Cy5-miR-124-3p (final conc. 25 nM) was performed with DharmaFECT Reagent (Thermo Fisher) following manufacturer's instructions.

2.4 | Glutamate Treatment

Prior to each experiment, a fresh 10 mM solution of L-glutamic acid (Sigma) in PBS was prepared. At DIV 7 (10 cm dishes) or DIV 9 (12 mm coverslips), the media was removed, and the cortical neuron cultures were rinsed with sterile PBS. Neurons were treated with 100 µM glutamate or with an equal volume of sterile PBS in NGM for 4 h at 37°C. The neuronal conditioned media (NCM) and cells were collected and stored at –80°C for further analysis.

2.5 | TUNEL Assay

TUNEL assay was performed with the One-step TUNEL In Situ Apoptosis Assay Kit (Elabscience) according to the manufacturer's instructions. ProLong Gold antifade reagent with DAPI (Invitrogen) was used for the nuclear counterstain.

2.6 | Immunostaining

For immunocytochemistry, hCD63-GFP^{fl/+} primary cortical neurons cultured on coated coverslips were washed once with PBS and fixed with 4% paraformaldehyde (PFA) for 15 min. Coverslips were rinsed three times in PBS followed by a solution of 0.2% Triton X-100 in PBS for 5 min. Then, the fixed permeabilised cells were incubated in blocking buffer (5% normal goat or donkey serum (NGS or NDS) and 0.1% Triton X-100 in PBS) for 1 h at room temperature. Primary antibodies for Rab7 (1:100, Cell Signaling #9367 or #95746), EEA1 (1:100, Cell Signaling #3288), Golga5 (1:100, Cell Signaling #A15768), mouse CD63 (1:50, Biolegend #143901) and β III-tubulin (1:1000, R&D Systems #MAB1195) were incubated overnight at 4°C in blocking buffer. After washing coverslips three times in PBS, corresponding secondary antibody in PBS (1:1000) was added for 2 h at room temperature. The cells were rinsed three times in PBS before mounting with ProLong Gold antifade reagent with DAPI (Invitrogen).

For immunohistochemistry, the animals were subjected to deep anaesthesia through intraperitoneal injection (i.p.) of a cocktail of Ketamine (100 mg/kg) and Xylazine (10 mg/kg) in saline, after which intracardial perfusion with 4% PFA in PBS was performed. The brains and spinal cords were dissected and kept in 4% PFA overnight at 4°C, then cryoprotected by immersion in 30% sucrose for 48 h. Tissues were embedded and frozen in Tissue-Tek OCT Compound (Sakura, Tokyo Japan). Coronal sections (20 or 40 μ m) were prepared with a cryostat (Leica HM525) and mounted on glass SuperFrost Plus slides (Fisher Scientific). For neuronal activity evaluation, slides were rinsed three times in PBS, then treated with blocking buffer (1% BSA, 5% goat-serum and 0.2% Triton-X-100 in PBS) for 45 min at room temperature and incubated with primary antibody for c-Fos (1:100, Cell Signaling #2250) overnight at 4°C in blocking buffer. After washing slides three times in PBS, corresponding secondary antibody was added for 2 h at room temperature. The sections were rinsed three times in PBS before mounting with ProLong Gold antifade reagent with DAPI (#P36931, Invitrogen). For visualisation of hCD63-GFP fluorescence, slides were washed three times in PBS before mounting with ProLong Gold antifade reagent with DAPI (#P36931, Invitrogen).

2.7 | Image Acquisition and Analysis

Imaging of hCD63-GFP neurons was performed using the Leica Falcon SP8 confocal laser scanning microscope (5–8 μ m Z-stack, 0.5 μ m step) magnified with $\times 63$ oil-immersion objective. Images were imported into FIJI (ImageJ2 version 2.14.0/1.54f) for further analysis. For hCD63-GFP^{fl/+} puncta distance quantification from nucleus, single neurons were isolated by drawing regions of interest (ROIs) of β III-tubulin. Blue (DAPI) and green (GFP) channels were converted into binary images and a threshold value

was applied for each one. To determine the X/Y coordinates of nucleus and hCD63-GFP^{fl/+} particles, the centre of mass was measured by selecting the Analyze Particle option. Using the Euclidean distance formula, the distance from hCD63-GFP^{fl/+} particles to the nucleus centre of mass was calculated. Distances were averaged per cell. Subcellular distribution of hCD63-GFP^{fl/+} puncta was calculated as a percentage of the total thresholded GFP signal area found on an individual neuron, defined by the β III-tubulin ROI. ROIs for soma and neurites were manually drawn and the GFP^{fl/+} signal area was measured on each ROI. GFP co-localisation analysis with EEA1, Rab7 or Golga5 was performed on every stack of single cells using the BIOP JACoP plugin. For this, ROI of β III-tubulin was defined, and the channels of interest were thresholded. Then, the thresholded M1 Mander's coefficients were obtained. The co-localisation between Rab7 and Golga5, or Cy5-miR-124-3p with hCD63-GFP was calculated as described, except that the neuron ROI was based on the DIC channel. Imaging of the TUNEL assay was performed in a Nikon Eclipse Ts2 inverted microscope with a 10 \times objective lens. The total number of cells (DAPI^{fl/+}) and dead cells (DAPI^{fl/+}TUNEL^{fl/+}) were obtained using the Cell Counter tool in Fiji and the percentage of dead cells was calculated.

For representative whole brain images, 10 \times objective magnification images were captured using a Keyence BZ-X microscope and stitched together, while c-Fos images were taken with the Zeiss Axio Imager at 10 \times magnification. Analysis was performed with FIJI. For the quantification of hCD63-GFP^{fl/+} brain tissue area, GFP intensity was first thresholded and ROIs containing signal were manually drawn on each side of the brain sections and their areas were measured. c-Fos immunostaining was quantified by setting an intensity threshold and the Integrated Density was measured. The values obtained for Control and hM3Dq brain sides were then normalised with the corresponding averaged Control value, and the percentage change between hM3Dq and Control side was calculated for each animal.

DAT-Cre^{fl/+}hCD63-GFP^{fl/+}Ai14-tdT^{fl/+} whole brain representative images at P40 were taken with the Keyence BZ-X microscope at 10 \times magnification and stitched together, while Zeiss Axio Imager at 10 \times magnification was used to image HB9-Cre^{fl/+}hCD63-GFP^{fl/+}Ai14-tdT^{fl/+} whole spinal cord representative image at E12. Confocal 40 \times magnification images were captured with the Nikon A1R (15–20 Z-stack, 0.5 μ m step size) and were utilised for the co-localisation analysis between hCD63-GFP and tdT.

2.8 | ImmunoEM Microscopy

Mice were deeply anaesthetised and transcardially perfused with ice-cold heparinised PBS followed by fixation with 4% PFA + 0.25% glutaraldehyde in PBS. Brains were dissected, post-fixed overnight at 4°C, and transferred to PBS. A total of 100 μ m coronal sections were cut on a vibratome and collected in PBS. Human CD63-GFP^{fl/+} cortical neurons cultured on precoated coverslips were fixed with 4% PFA + 0.25% glutaraldehyde in PBS. Brain sections and neuron samples were processed for 5 nm immunogold labelling of GFP (anti-turbo GFP, Evrogen #AB513) at the Harvard Medical School Electron Microscopy Core facility. Images were acquired on a JEOL 1200EX transmission electron microscope. The number of axon terminals and dendritic

spines containing immunogold particles (threshold for positive labelling: >1 immunogold particle) versus lacking immunogold particles within synapse-containing images were expressed as percentages.

2.9 | EV Purification and Nanoparticle Tracking Analysis

EVs from NCM (5×10^6 cells/10 cm dish) were isolated by size exclusion chromatography using the IZON qEV original/35 nm columns following manufacturer's instructions. Prior to the isolation process, the NCM was first spun at $300 \times g$ for 10 min to remove cell debris, $4000 \times g$ for 10 min at 4°C , and then concentrated with Centricon Plus-70 filter (10K MWCO, Millipore) at $3500 \times g$ at 4°C until a volume of 500 μL or less was obtained. The concentrated sample was then transferred into the IZON column for separation. Fractions containing EVs (#7 to #9) were combined and concentrated through Amicon Ultra-4 filter unit, and the final volume was adjusted to 100 μL for all samples. Extracellular vesicle size and concentration were analyzed by nanoparticle tracking analysis using the ZetaView instrument (Particle Metrix) and corresponding software ZetaView (version 8.05.11 SP1) at the Boston Children's Hospital Cell Function and Imaging Core, Harvard Digestive Diseases Center (Boston, MA). Firstly, 100 nm 'Standard beads' (Particle Metrix GmbH) were used to calibrate the machine. The following settings were used for all measurements: 11 positions, 2 cycles, minimal brightness of 18, minimal size of 10 nm and trace length of 10 s. Sample dilutions were adjusted using milliQ water to a final volume of 1 mL.

2.10 | Immunoblotting

Anti-mouse CD63 (1:500, Abcam #ab217345), anti-human CD63 (1:100, Santa Cruz #sc-5275), anti-CD81 (1:400, Santa Cruz #sc-166029), anti-Alix (1:100, Santa Cruz #sc-53540), anti-turbo GFP (1:1000, Evrogen #AB513), anti-EEA1 (1:1000, Cell Signaling #3288), anti-Rab7 (1:1000, Cell Signaling #9367), anti-Arc (1:10000, Proteintech #66550) and anti-GAPDH (1:10000, Proteintech #60004-1-Ig) primary antibodies were used. Neuronal pellets and EV fractions were homogenised with RIPA buffer (Thermo Scientific). Protein inhibitor cocktail (P8340, Sigma) was added in a 1/100 dilution to this lysis buffer prior to sample homogenisation. Total protein amount of cell lysates was determined by DC protein assay (Bio-Rad). Forty micrograms of neuronal lysate or equal volumes of EV lysate were prepared with sample buffer 4X (Bio-Rad) and β -mercaptoethanol, heated at 95°C for 5 min and loaded on stain-free 4%–15% gradient sodium dodecyl sulphate polyacrylamide gel electrophoresis gels (Bio-Rad). Separated proteins were transferred onto a Polyvinylidene difluoride (PVDF) membrane using the Trans-Blot Turbo system (Bio-Rad). The membrane was blocked with 5% non-fat dry milk in TBST (Tris buffered saline with 0.1% Tween 20) then incubated with the appropriate primary antibody overnight at 4°C . On the following day, the membrane was exposed to HRP-conjugated goat anti-rabbit or anti-mouse secondary antibody (1:10,000) diluted in TBST. Bands were visualised using the ChemiDoc MP imaging system (Bio-Rad) by ECL chemiluminescent substrate (Clarity Max Western ECL Substrate, Bio-Rad). Exposure time was optimised for detecting different proteins.

2.11 | RNA Isolation and miR qPCR

Total RNA was extracted from EV fractions and neuronal cell pellets using TRIzol reagent (Invitrogen) by following the manufacturer's instructions. RNA concentration was measured using the NanoDrop ND-1000 UV-Vis Spectrophotometer. Equal quantities (10 ng) of each sample were used to convert the miRs into cDNA using the TaqMan MicroRNA Reverse Transcription Kit (Applied Biosystems) with specific primers for each individual miR (included in each TaqMan MicroRNA Assay) and control U6 small nuclear (sn) RNA (Applied Biosystems; used for neuronal samples only). qPCR was performed in a StepOnePlus Real-Time PCR system (Applied Biosystems) with matching miR probes (TaqMan MicroRNA Assay) and TaqMan $2\times$ Universal PCR Master Mix. Within each individual sample, the abundance of each miR was calculated relative to miR-9-5p, the most abundant neuronal miR. To determine the relative enrichment of individual miR in neuronal EVs over its neuronal abundance, an EV miR Enrichment index was calculated by dividing the EV fold change of a particular miR (relative to miR-9-5p) by its corresponding neuronal fold change (relative to miR-9-5p).

2.12 | Small RNA Sequencing and Analysis

Small RNA sequencing was performed at Tufts University Core Facility Genomics Core (Boston, MA). The quantity and quality of isolated EV RNA was determined using the Agilent 5200 Fragment Analyzer system. Library preparation was done with the QIAseq miRNA Library Kit (Qiagen), and the Illumina NovaSeq 6000 instrument was used for sequencing. The small RNA-seq data was analysed at the University of Texas Health Science Center at Houston, McGovern Medical School (Houston, TX). Data pre-processing involved the removal of adapter, index and low-quality reads using cutadapt (DOI: 10.14806/ej.17.1.200). Subsequently, small RNA with sizes ranging from 17 to 40 nucleotides were selected for further analyses. Alignment of these small RNA was performed against mature miRNA sequences of mice sourced from miRbase using bowtie (<https://doi.org/10.1186/gb-2009-10-3-r25>). Samtools (<https://doi.org/10.1093/bioinformatics/btp352>) sorted the aligned reads to mature miRNA sequences and generated read counts for each miRNA. Normalisation of miRNA raw reads was performed using Deseq2 (PMID: 25516281) with default parameter. Differential gene expression analysis was conducted using DESeq2 with identification of significant differentially expressed miRs based on criteria including an adjusted p value less than 0.05 and a fold change greater than 2.

2.13 | Bioinformatic Prediction of miR/mRNA Binding

Predicted mRNA targets of top detected miRs in EVs were determined using TargetScan Mouse 8.0. Targets with >1 conserved site were considered. The list of predicted targets was cross-referenced with datasets from Zhang et al. 2014 (neurons, microglia, oligodendrocytes and endothelial cells) and Morel et al. 2017 (adult astrocytes) to determine cell-type specific mRNA transcripts, using thresholds of FPKM > 10 and > 4-fold enrichment relative to all other cell types.

2.14 | Stereotaxic Delivery of AAV Virus

A mixture of AAV8-hSyn-DIO-hM3Dq-mCherry (1.5 μ L, 3.20×10^{13} gc/mL) (Addgene, #44361) and AAV9-hSyn-Cre-hGH (0.5 μ L, 2.30×10^{13} gc/mL) (Addgene, #105555) was stereotaxically injected into the motor cortex of the right hemisphere of hCD63-GFP^{f/+} mice (Bregma 0, M/L = 1.0 mm, D/V = -1.0 mm). A mixture of AAV9-hSyn-Cre (0.5 μ L, 1×10^{13} gc/mL) and PBS (1.5 μ L, 1X) was stereotaxically injected into the motor cortex of the left hemisphere of hCD63-GFP^{f/+} mice (Bregma 0, M/L = -1.0 mm, D/V = -1.0 mm). AAV8-Syn-DIO-hCD63-GFP virus (0.6 μ L, 1.31×10^{14} gc/mL) was injected bilaterally in the ventral tegmental area (VTA) of DAT-Cre mice (A/V = -3.1 mm from Bregma, M/L = \pm 0.75 mm, D/V = -4.7 mm). AAV8-Syn-DIO-hCD63-GFP virus was packaged by the Boston Children's Hospital Viral core (Boston, MA). Mice were anaesthetised with isoflurane vapour (Covetrus). Post-operative care included injections of buprenorphine according to the IACUC requirement. Animals were perfused 14 days after injections.

2.15 | Statistical Analysis

Data sets were analysed using GraphPad Prism 10.1.1 software (La Jolla, CA, USA) and presented as mean \pm SEM. Data sets were compared using two-tailed Student's *t*-tests or one- and two-way ANOVA with post-hoc Šidák post-hoc testing unless otherwise indicated. Statistical significance was tested at a 95% ($p < 0.05$) confidence level and *p* values were shown in each graph.

3 | Results

3.1 | Glutamatergic Signalling Regulates Compartmental and Subcellular Trafficking of Tetraspanin CD63 in Cortical Neurons

We previously generated hCD63-GFP^{f/f} mice to selectively and efficiently label secreted exosomes and their intracellular precursor ILVs in a cell-type specific manner by tagging the C-terminus of exosome (but not MV) surface marker human (h) CD63 with the GFP reporter (Men et al. 2019). AAV-CaMKII-Cre induced hCD63-GFP expression has a peri-nuclear localisation pattern in neuronal soma (Figure 1Aii) which is highly similar and well overlapped (>70%) with endogenous mouse (m) CD63 immunoreactivity (Figure 1Ai,B). For acute glutamate treatment (up to 4 h), glutamate (100 μ M), comparable to evoked synaptically released glutamate concentration in previous studies (Herman and Jahr 2007), was added to cortical neuronal cultures at days in vitro 7 (DIV7) when glutamate receptors are evidently expressed (Ha et al. 2009). Glutamate stimulation of neurons induced minimal additional neuronal cell death compared to control within 4 h based on TUNEL staining (Figure 1C), consistent with previous report (Ha et al. 2009). The overlap between endogenous mCD63 and hCD63-GFP is only slightly affected by acute glutamate treatment for up to 4 h (Figure 1B). Similarly, glutamate stimulation induced no expression changes of hCD63, mCD63, GFP and other ILV marker CD81 (Figure 1D,E). Note that hCD63 is not recognised by the mCD63 antibody on the immunoblot (red arrow, Figure 1D). Interestingly, glutamate stimulation significantly increased the mean distance between all

hCD63-GFP⁺ puncta to the centre of nucleus (Figure 1Fi-ii,G), suggesting an increasingly scattered distribution of hCD63-GFP signals from neuronal soma to the whole neuron. Consistently, glutamate stimulation significantly reduced the total hCD63-GFP⁺ puncta area in soma while increasing that in neurites (yellow arrows in Figure 1Fii, quantification in Figure 1H). As there are no obvious expression changes of hCD63 and GFP induced by glutamate stimulation (Figure 1D,E), it is unlikely that increased scattering of hCD63-GFP⁺ puncta by glutamate is due to hCD63-GFP expression changes.

As CD63 is a well-validated exosome (but not MV) surface marker (Kowal et al. 2016), its subcellular localisation facilitates the examination of subcellular localisation of ILVs, especially within the endosome/lysosome network (ELN). Currently, how CD63 is trafficked intracellularly in neurons remains unknown. Although it is a predicted plasma membrane protein like other tetraspanin family members (Pols and Klumperman 2009), we observed no hCD63-GFP signal on the neuronal surface, nor with the mCD63 immunostaining (Figure 1). To further characterise CD63 intracellular trafficking, we then performed immunostaining of EEA1 and Rab7, selective markers for early endosome and multivesicular body (MVB) respectively in hCD63-GFP induced primary neurons following glutamate stimulation (Figure 2A). As the ER/Golgi network is able to directly deliver newly synthesised and modified proteins to endosomal compartments, we also performed immunostaining of Golga5 that selectively labels the Golgi network (Figure 2A). Quantitative co-localisation of hCD63-GFP with these organelle markers showed predominant co-localisation of hCD63-GFP with MVB marker Rab7 ($78 \pm 2\%$), but only $\sim 7 \pm 0.5\%$ overlap with early endosome marker EEA1, $\sim 15 \pm 1.1\%$ with Golgi marker Golga5, and $<1\%$ with DAPI (Figure 2Ai-iii, i'-iii',B), indicating that MVBs are the primary source of hCD63-GFP⁺ ILVs. Interestingly, glutamate stimulation had minimal effect on the co-localisation of hCD63-GFP with EEA1, Golga5 (Figure 2Ai',iii',B) and DAPI, but significantly reduced co-localisation of hCD63-GFP with Rab7 (Figure 2Aii',B), even a significantly increased Rab7 protein expression upon glutamate stimulation was observed (Figure 2C,D). Meanwhile, EEA1 protein expression was significantly decreased upon glutamate stimulation (Figure 2C,D), which may correspond to altered transition of early endosomes into MVBs by glutamate stimulation during endosome maturation. As hCD63-GFP is localised on the surface of MVB-derived ILVs, its reduced co-localisation with Rab7 by glutamate stimulation suggests that glutamate stimulation may induce release of ILVs from the MVB to extracellular space. This is in parallel with glutamate-induced increasingly scattered localisation of hCD63-GFP in neurons that presumably suggests their trafficking near the plasma membrane for release.

In addition, substantially higher co-localisation of hCD63-GFP with Golga5 ($\sim 15 \pm 1.1\%$, Figure 2B) than co-localisation of hCD63-GFP with EEA1 ($\sim 7 \pm 0.5\%$, Figure 2B) also suggests that a portion of newly synthesised hCD63-GFP traffics directly from Golgi networks to MVBs without being first targeted to the plasma membrane and subsequently endocytosed into early endosomes. Indeed, a similar percentage of co-localisation between Rab7 and Golga5 ($\sim 13 \pm 1\%$, Figure 2E,F) was also observed. The co-localisation between Golga5 and Rab7 (Figure 2F) is not altered by glutamate stimulation. To overcome

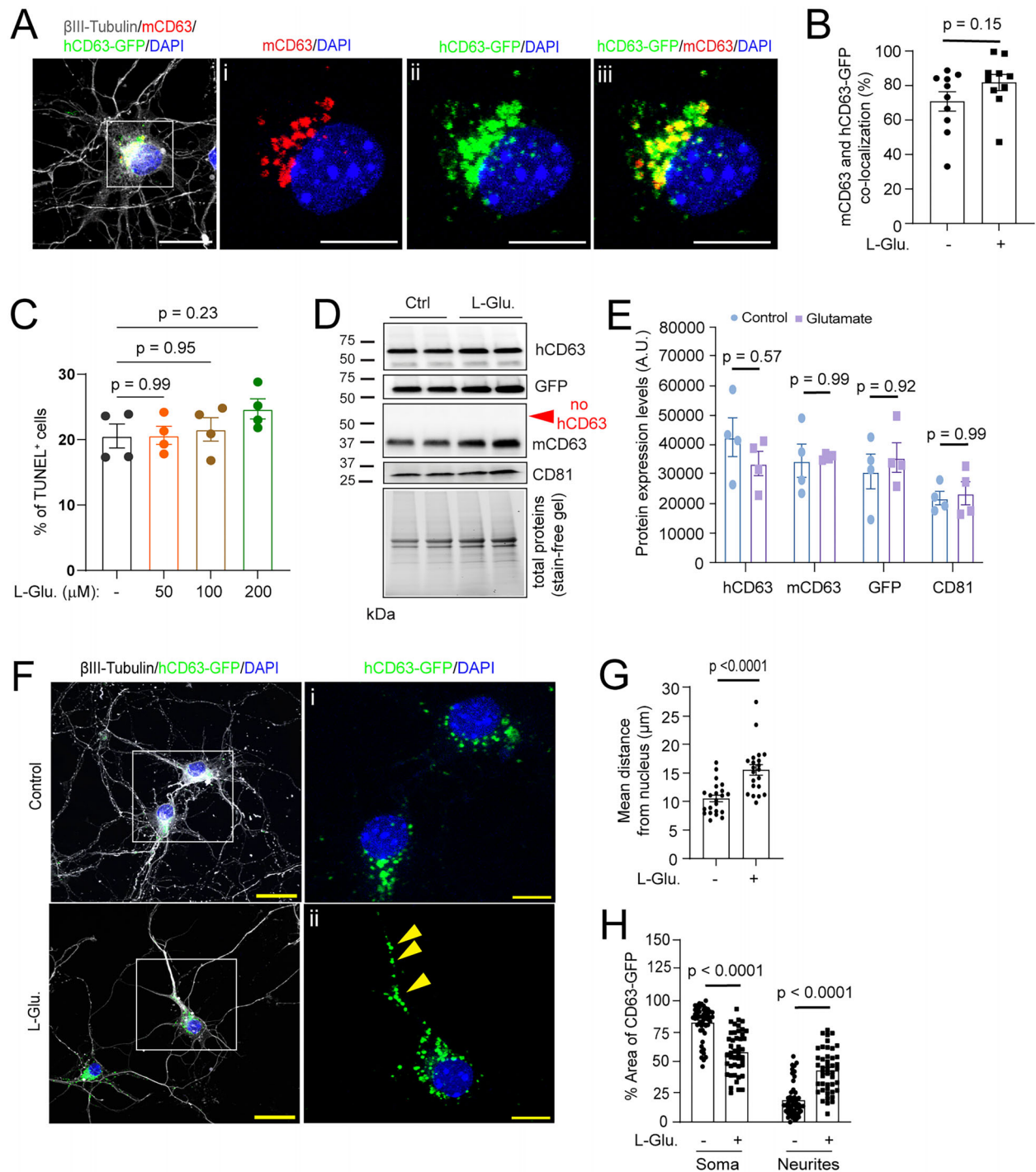


FIGURE 1 | Glutamatergic signalling regulates compartmental localisation of tetraspanin CD63 in cortical neurons. (A) Representative confocal images of hCD63-GFP neurons with endogenous mouse CD63 immunoreactivity. Scale bar: 20 μ m, 10 μ m (i–iii). (B) Quantitative analysis of co-localisation comparison between control and glutamate (L-Glu.) treatment. $n = 10$ –11 neurons/group; p values determined in two-tailed unpaired t test. (C) TUNEL assay in L-Glu.-treated neurons. $N = 20$ fields from 4 cultures/group. p values determined in one-way ANOVA and post hoc Dunnett’s multiple comparison test. Representative immunoblots (D) and quantification (E) of engineered exosome markers (hCD63, GFP) and endogenous exosome markers (mCD63, CD81) in whole neuronal cell lysates (WCL). Note that mCD63 antibody detects no hCD63 signals (red arrow). $n = 4$ independent samples/group. Protein expression levels were normalised by total loaded proteins (stain-free gel). p values determined in one-way ANOVA with Tukey’s post hoc analysis. (F) Representative confocal images of the subcellular distribution of hCD63-GFP⁺ puncta in cultured primary neurons following glutamate treatment. Yellow arrows: hCD63-GFP signals in neurites. Scale bar: 30 and 10 μ m (magnified view). (G) Quantification of hCD63-GFP⁺ puncta distance from nucleus in control and glutamate treated neurons. $n = 21$ –22 cells/group; p values determined from the two-tailed unpaired t test. (H) Quantification of hCD63-GFP signal in soma and neurites, represented as a percentage of the total signal area found in the cell. $n = 40$ –50 neurons from four biological replicates per group; p values determined in the two-way ANOVA with post hoc Šidák test.

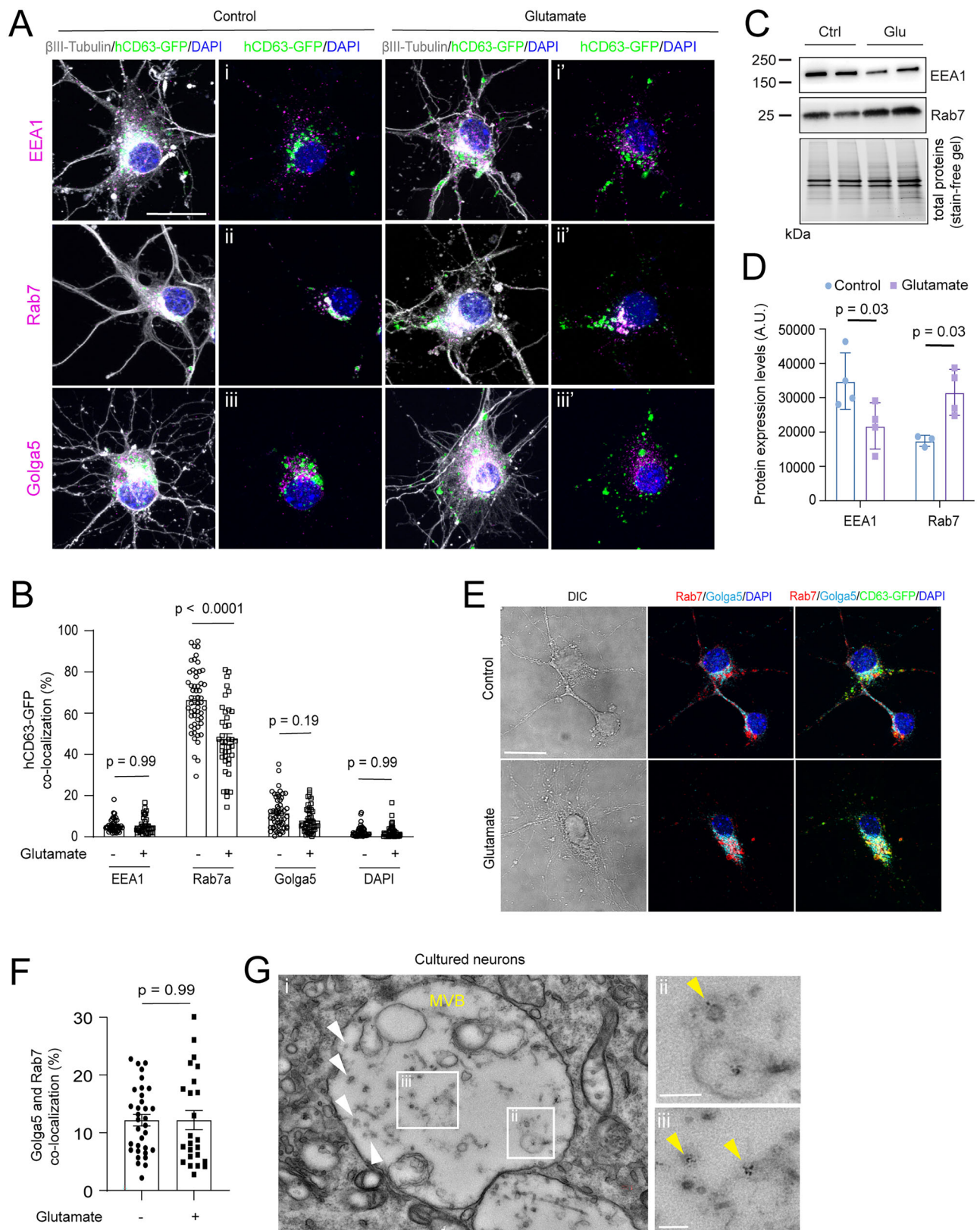


FIGURE 2 | Glutamate stimulation affects the endosomal pathway and subcellular trafficking of hCD63-GFP⁺ vesicles. (A) Representative confocal images of control and glutamate-treated (4 h) hCD63-GFP expressing neurons immunostained with EEA1 (early endosomes), Rab7 (late endosomes/MVBs) and Golga5 (Golgi apparatus) antibodies; Scale bar: 20 μ m. (B) Quantification of hCD63-GFP co-localisation with individual organelle markers in control and glutamate treated neurons. $n = 40$ –55 neurons from four biological replicates per group; p values determined from two-way ANOVA with post hoc Šidák test. Representative immunoblots (C) and quantification (D) of endosomal markers EEA1 (early endosomes) and Rab7 (late endosomes/MVBs) in whole neuronal cell lysates (WCL). Protein expression levels were normalised by total loaded proteins (stain-free gel). $n = 4$ independent samples/group, two-way ANOVA with post hoc Šidák test. (E) Representative DIC and confocal images of Rab7 and Golga5 immunostaining

the resolution limit of light microscopy, we further performed GFP immunogold labelling and EM imaging on hCD63-GFP⁺ cultured neurons. GFP⁺ immunogold vesicles (Figure 2Gii–iii) as well as inwardly budded small vesicles (Figure 2Gi), the ILVs, were observed within the MVB structure, clearly demonstrating MVB-originated exosome biogenesis in primary neurons, consistent with that in non-neural cells.

3.2 | Glutamatergic Signalling Significantly Promotes EV Secretion From Cortical Neurons But Only Modestly Alters miRNA (miR) Profile in Neuronal EVs

To directly examine how glutamate stimulation alters neuronal EV secretion, we collected neuron-conditioned medium (NCM) 4 h following glutamate treatment. Neuronal EVs were isolated by size exclusion chromatography (SEC) and their size and quantity were determined by ZetaView nanoparticle tracking analysis (NTA). EVs secreted from control and glutamate-stimulated neurons were highly similar in size distribution (Figure 3A). Interestingly, >98% vesicle size is typical of small EV size (50–200 nm), consistent with the predominant MVB localisation of hCD63-GFP in neurons. Glutamate stimulation increased EV numbers in almost all size ranges (Figure 3A), with a 45% increase in the total number of EVs secreted from glutamate-stimulated neurons compared to control neurons (Figure 3B). Subsequent immunoblotting detected engineered GFP and hCD63, as well as several other well-validated exosome markers mCD63, CD81 and Alix (Figure 3C), confirming that hCD63-GFP is indeed localised on the surface of exosomes, together with endogenous mCD63, to be secreted from neurons. On the other hand, CD9 was not detected in our EV samples (Figure 3C). These immunoblotting results support the notion that neuronal EVs are primarily originated from MVB (exosomes) but not from plasma membrane (MVs). Interestingly, although Arc has been shown to form a viral capsid-like structure to package its own mRNA (Pastuzyn et al. 2018), we detected no Arc in neuronal EVs (Figure 3C), possibly due to the heterogenous nature of secreted vesicles from neurons.

As miRs are considered a major category of cargoes in neuronal EV especially exosomes to mediate intercellular communications, we decide to first examine whether glutamatergic signalling alters miR content in neuronal EVs, which will reveal potential crosstalk between these two communication mechanisms. We sequenced small RNAs isolated from EVs purified from control and glutamate-treated neuronal cultures. The overall mean counts and number of detected miRs were highly similar in both groups (Figure 3D). In addition, the very top detected miRs (mean counts > 10⁵), miR-125b-5p, miR-9-5p, miR-128-3p and so forth, were also highly conserved in both control and glutamate-stimulated neuronal EVs with no differences in mean counts (Figure 3E). Out of ~750 total detected miRs, 18 and 5 were significantly ($p < 0.05$, FC > 2) up- and down-regulated in neuronal EVs by the glutamate stimulation, respectively (Figure 3F,G).

We further examined the abundance of top detected EV miRs and miR-124-3p (also within 10% detected miRs in EVs) based on our previous studies (Men et al. 2019; Morel et al. 2013) in neurons and neuronal EVs, by quantitative PCR, to determine their relative enrichment in EVs. Currently, it is undetermined as to which small RNAs can be considered “housekeeping” that are reliably packaged into neuronal EVs and can be used to normalise relative abundance between cellular and EV miRNAs. Therefore, we decide to use miR-9-5p (most abundant in tested miRs) as the reference for relative comparison across different miRs in either neuron or EV samples by calculating the EV miR Enrichment index (as described in Section 2). Although miR-9-5p was highly expressed and far more abundant than miR-124-3p in neurons (Figure 4A), it was less proportionally abundant in EVs (Figure 4B) compared to miR-124-3p with a much lower EV miR Enrichment index (Figure 4C). These results indicate that certain miRs were differentially enriched in EVs regardless their neuronal abundance (Figure 4C). These results also support a selective sorting mechanism in packaging certain miRs into ILVs in neurons. Interestingly, glutamate stimulation had no major impact on miR abundance in neurons and EVs (Figure 4A,B), indicated by the similar miR enrichment in neuronal EVs after glutamate treatment (Figure 4C).

To examine whether miR cargoes are indeed packaged into ILVs inside neurons, we transfected hCD63-GFP⁺ primary cortical neurons with Cy5-labeled miR-124-3p, one of the highly detected miRs in neuronal EVs and is functionally significant in mediating neuron to astroglia communication (Men et al. 2019; Morel et al. 2013), to examine its co-localisation with hCD63-GFP⁺ ILVs inside neurons. Transfected Cy5-miR-124 was primarily localised within neuronal soma near the nucleus (Figure 4D), similar to the subcellular distribution of hCD63-GFP. Indeed, a high percentage ($68 \pm 6.4\%$) co-localisation between Cy5-labelled miR-124-3p and hCD63-GFP⁺ ILVs was observed in neurons (Figure 4E), confirming its substantial packaging into ILVs. Glutamate stimulation only slightly reduces co-localisation of Cy5-miR-124-3p with hCD63-GFP ($p = 0.15$, Figure 4E), consistent with the modest effect of glutamate on EV miR profile observed above. As EV miRs have been shown to mediate a number of functions intercellularly, including in the CNS, we then analyzed whether certain top detected miRs preferentially target on mRNAs that are selectively expressed or enriched in specific CNS cell types (Figure 4F) based on previously published CNS cell type transcriptome databases (Morel et al. 2017; Zhang et al. 2014). Our analysis showed that miR-128-3p is predicted to bind to the largest number of neuron-selective mRNAs (Figure 4G) and miR-125b-5p preferentially targets on microglial mRNAs (Figure 4H), while miR-9-5p preferentially targets on endothelial cell mRNA (Figure 4I) (also see the Supplemental table). The selective targeting of cell-type specific mRNAs by different highly detected EV miRs suggests potentially pleiotropic functions of neuronal EVs.

in control and glutamate-stimulated hCD63-GFP⁺ neurons. Scale bar: 20 μ m. (F) Quantitative analysis of co-localisation between Rab7 and Golga5 in control and glutamate-stimulated hCD63-GFP⁺ neurons. $n = 24$ –33 neurons/group; two-tailed unpaired t test. (G) Representative electron-microscopy images of immunogold labelling of GFP in MVB in cultured cortical neurons and magnified views of GFP⁺ intraluminal vesicles (yellow arrows); White arrows: ILVs in MVB; Scale bar: 100 nm.

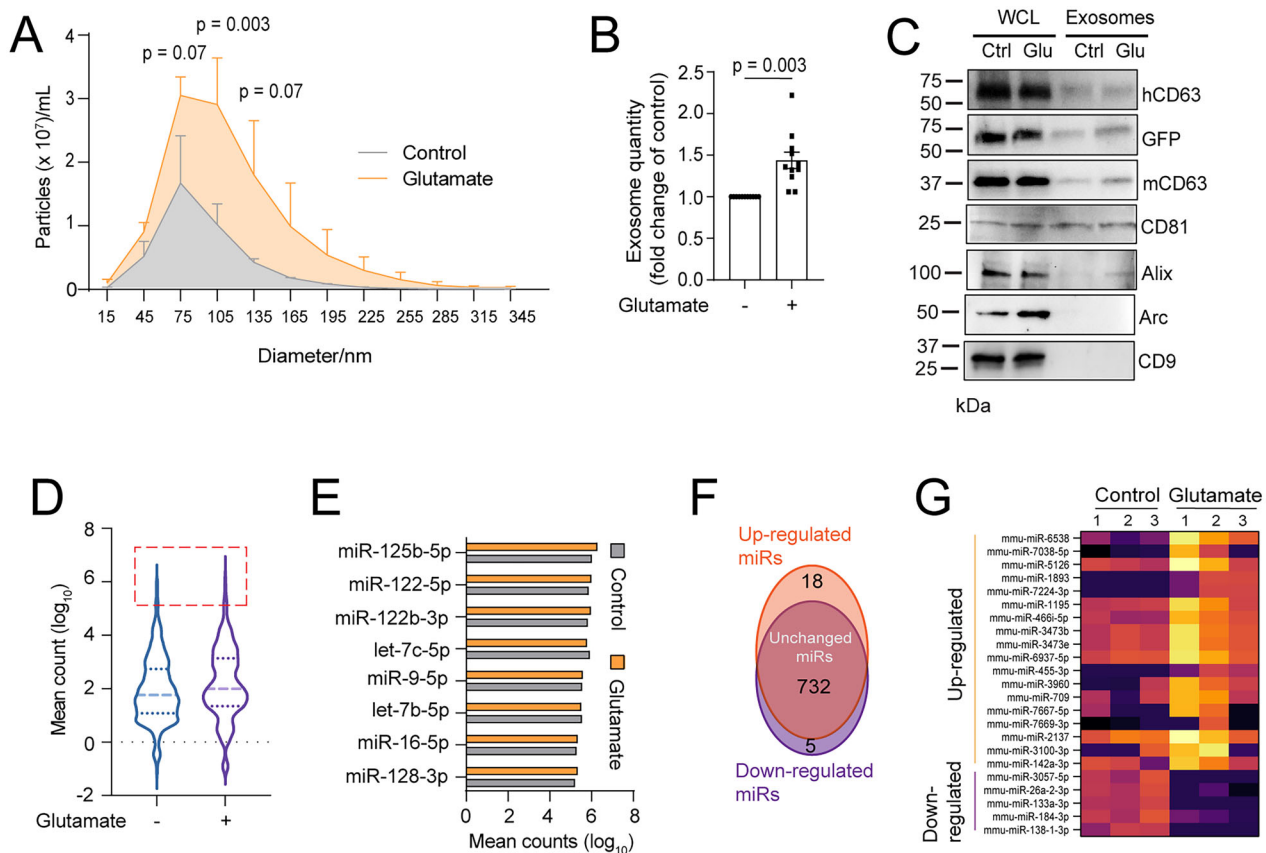


FIGURE 3 | Glutamate stimulation significantly promotes EV secretion from cortical neurons but only modestly alters miRNA (miR) profile in neuronal EVs. (A) Representative size distribution of EVs isolated from conditioned medium of control and glutamate treated cultured primary neurons. $n = 3$ replicates; p values determined from two-way ANOVA with post hoc Šidák test. (B) Relative fold change (over untreated control) of NTA measured total secreted EVs from control and glutamate-treated neurons. $n = 11$ individual replicates/group; Measured EV numbers are within 10^8 – 10^9 particles/mL. p values determined from two-tailed unpaired t -test. (C) Representative immunoblots of engineered GFP tag, human CD63 and other typical EV protein markers from hCD63-GFP⁺ whole cell lysate (WCL) and purified EVs. (D) Violin plot depicting the distribution of all detected miRNAs in EVs isolated from control and glutamate-treated neurons. The mean count from each group (three replicates/group) was converted (\log_{10}). Highly expressed miRNAs in both conditions are indicated by the red rectangle and graphed in (E). (F) Venn diagram of glutamate-induced up-, down-regulated and unchanged EV miRNAs determined by small RNA-seq analysis; Up- and down-regulated miRNAs were identified based on $padj < 0.05$ and fold change > 2 . (G) Heatmap showing the up- and down-regulated EV miRNAs ($padj < 0.05$, \log_{10} mean counts) from cultured primary cortical neurons after glutamate exposure. $n = 3$ replicates/group.

3.3 | In Vivo Neuronal Excitation Promotes Spreading of Cortical Neuron-Secreted EVs

Whether neuronal activity influences spreading of neuronal EVs in vivo remains unexplored. We decided to address this question by employing the DREADD-based chemogenetic approach to precisely modulate activity of targeted neurons following administration of DREADD selective agonist CNO. We were particularly interested in the effect of neuronal excitation on EV secretion and spreading, which can be more clearly assessed than inhibition from targeted neurons. The overall injection paradigm and experimental groups are illustrated in Figure 5A, in which AAV-hSyn-Cre or a mixture of AAV-hSyn-Cre and AAV-DIO-hM3Dq-mCherry are separately and focally injected into the motor cortex of hCD63-GFP^{+/+} mice (Figure 5A). In this paradigm, focal injections of equal AAV-hSyn-Cre virus leads to parallel hCD63-GFP induction from both cortical sides, while the mCherry-tagged hM3Dq receptor is only induced in neurons on one cortical side injected with the mixture of AAV-hSyn-Cre

and AAV-DIO-hM3Dq-mCherry. As a result, hCD63-GFP⁺ areas, indication of ILVs and secreted exosomes from neurons, can be visualised and compared following DREADD-mediated neuronal activation.

The AAV-hSyn-Cre and AAV-DIO-hM3Dq-mCherry virus titer and CNO dose/duration have been tested to achieve optimised hCD63-GFP and hM3Dq-mCherry induction and neuronal excitation. As expected, hM3Dq-mCherry was found only on the side with the AAV-hSyn-Cre/AAV-DIO-hM3Dq-mCherry injection (Figure 5Bii), while hCD63-GFP signals were observed on both cortical sides (Figure 5Bi-ii). Subsequent c-Fos immunostaining also showed clear c-Fos immunoreactivity only in mCherry⁺ neurons (yellow arrows, Figure 5Bii-a,b,e) but not in control mCherry⁻ neurons (Figure 5Bi-a,c,e), confirming hM3Dq-mediated neuronal activation in these neurons. AAV-hSyn-Cre-induced GFP signals were also clearly observed inside the same mCherry⁺ neurons (Figure 5Bii-d,ii-e). The co-localisation of hCD63-GFP and mCherry in the neuron was also shown

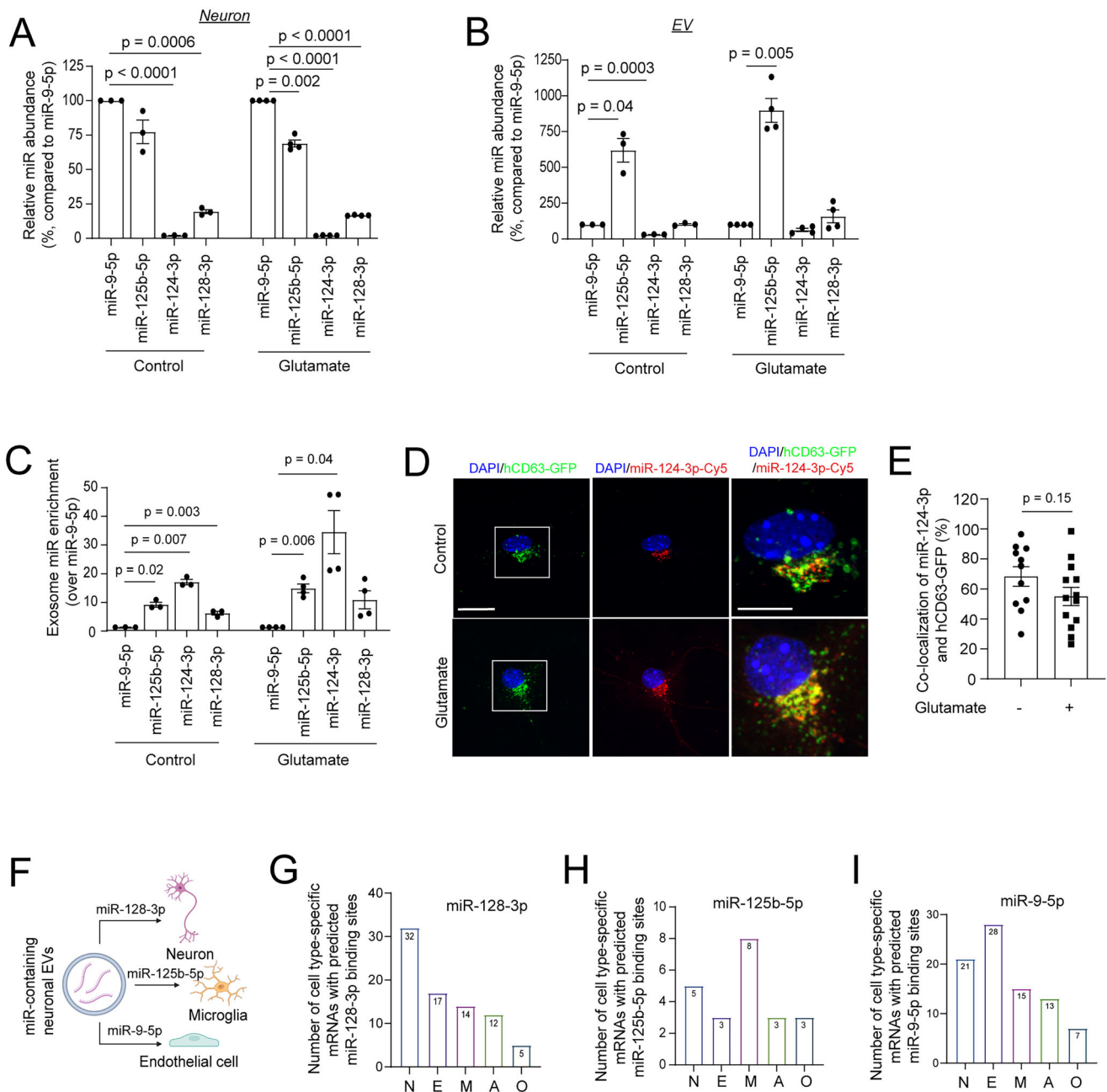


FIGURE 4 | Neuronal miRs are differentially enriched in neuronal EVs with minimal impact by glutamate stimulation. Relative miR abundance (% in comparison to miR-9-5p) in neurons (A) and EVs (B) in both control and glutamate stimulated neurons. $n = 3-4$ independent cultures/group; p values determined from repeated measures one-way ANOVA with Dunnett's multiple comparisons test. (C) Relative enrichment of miRs into EVs (fold change in comparison to miR-9-5p) from control and glutamate stimulated neurons. miR abundance in neurons and EVs was determined using qPCR and individually normalised to each sample's miR-9-5p level which is most abundant in neurons. $n = 3-4$ independent cultures/group; p values determined from repeated measures one-way ANOVA with Dunnett's multiple comparisons test. (D) Representative confocal images of transfected Cy5-miR-124-3p in control and glutamate-treated hCD63-GFP⁺ neurons; Scale bar: 20 and 10 μ m (magnified view). (E) Quantification of co-localisation between Cy5-miR-124-3p and hCD63-GFP⁺ puncta in control and glutamate treated neurons. $n = 11-13$ neurons/group; p value determined from the two-tailed unpaired t test. Schematic diagram (F) of potential targeted delivery of miR-128-3p, miR-125b-5p and miR-9-5p to neurons (G), microglia (H) and endothelial cells (I), respectively, based on the number of cell type-enriched predicted targets showed in the graphs. Predicted mRNA targets of top detected miRs in EVs were determined using TargetScan Mouse 8.0. Targets with >1 conserved site were considered. Cell-type specific mRNA transcripts were determined with thresholds of FPKM > 10 and > 4 -fold enrichment relative to all other cell types.

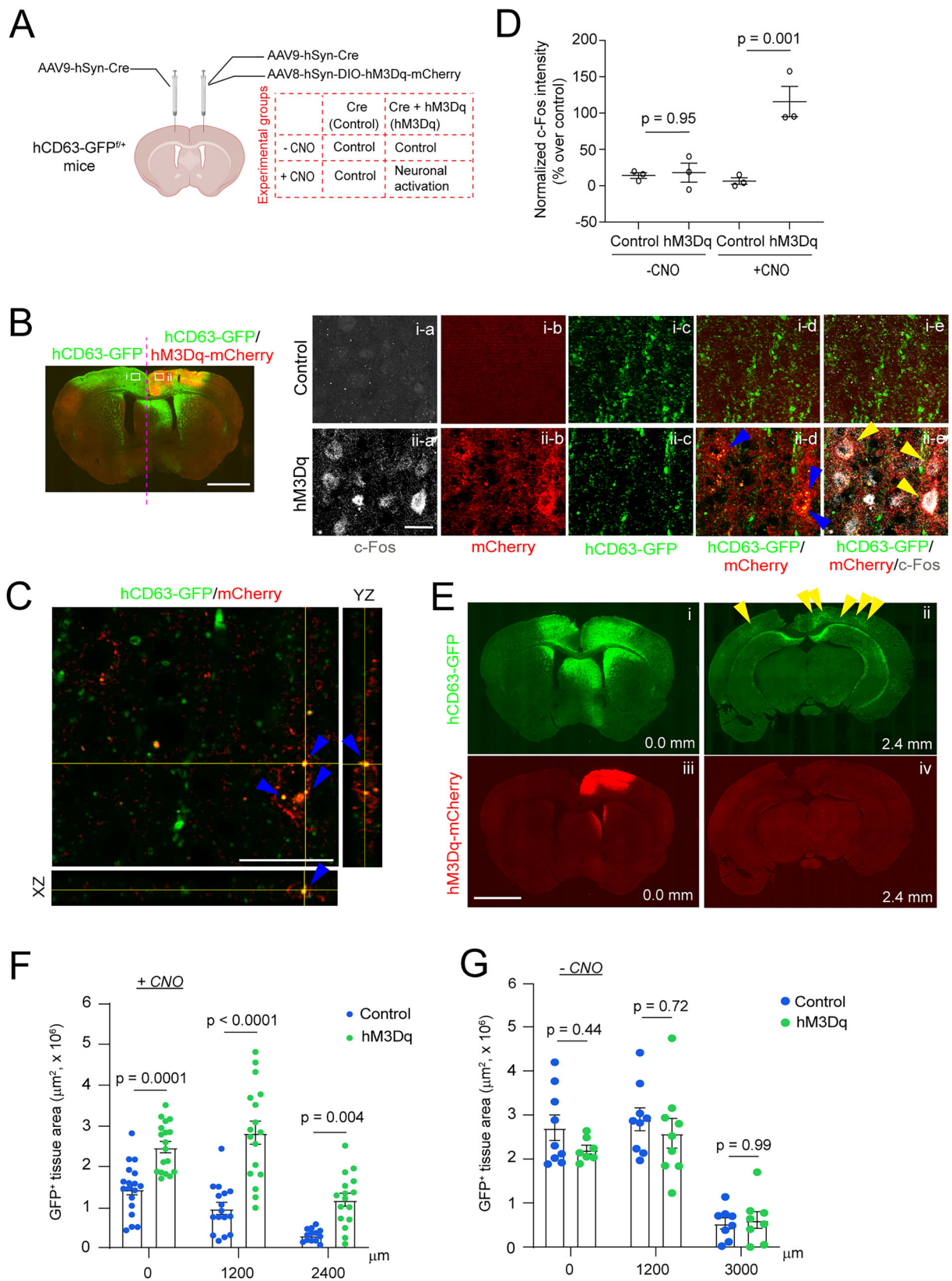


FIGURE 5 | In vivo DREADD-mediated neuronal excitation promotes spreading of hCD63-GFP⁺ exosomes secreted from cortical neurons. (A) Experimental diagram and groups of bilateral and focal AAV injections into the motor cortex of hCD63-GFP^{+/+} mice. One cortical side received a mixture of AAV8-DIO-hM3Dq-mCherry and AAV9-hSyn-Cre virus, and the contralateral cortical side was injected with only AAV9-hSyn-Cre virus as a control. Experimental groups were also shown. (B) A representative image of the bilateral injection and magnified view of both cortical sides (i: control side; ii: hM3Dq side, scale bar = 1 mm and 30 μ m (magnified views, ia-ie and iia-ii-e) following CNO administration and c-Fos immunostaining. Yellow arrows

in the orthogonal view from the single Z-focal plane (yellow arrows, Figure 5C). Quantification of c-Fos immunoreactivity found substantial and selective increase only on the AAV-hSyn-Cre/AAV-DIO-hM3Dq-mCherry-injected cortical side with CNO administration (Figure 5Bii,D) but not on the AAV-hSyn-Cre-injected side or without CNO (Figure 5D), confirming the specific excitation effect of hM3Dq/CNO on cortical neuronal activity. Subsequent quantification of hCD63-GFP⁺ area found a consistently and significantly greater hCD63-GFP⁺ tissue area at both proximal (0.0 mm, Figure 5E) and distant (2.4 mm, Figure 5E) sections from the injection site in the AAV-hSyn-Cre/AAV-DIO-hM3Dq-mCherry-injected cortical side compared to AAV-hSyn-Cre-injected cortical side following CNO administration (Figure 5F), but not without CNO administration (Figure 5G). These in vivo DREADD-mediated neuronal excitation results are consistent with glutamate-stimulated EV secretion in cultured cortical neurons, further supporting the notion that increased neuronal excitation promotes EV secretion and spreading.

3.4 | In Vivo Illustration of Intracellular hCD63-GFP⁺ ILVs and hCD63-GFP⁺ EVs From Specialised Neuronal Subtypes and Regions in the CNS

In vivo illustration of neuron-secreted EVs in the CNS remains very limited. By generating cell-type specific and inducible ILV/exosome reporter mice, we previously began to demonstrate the in situ localisation of exosomes secreted from forebrain (CaMKII⁺) excitatory neurons in adult mice with confocal and immunoEM imaging (Men et al. 2019). Given the presence of highly diverse neuronal subtypes in the mammalian CNS, we set out to explore in situ localisation of CD63⁺ ILVs/exosomes from other representative neuronal subtypes such as Homeobox transcription factor (HB9⁺) motor neurons (MNs) in the spinal cord and dopamine transporter (DAT⁺) dopaminergic neurons from midbrain. These neuronal subtypes were chosen based on their predominant ventral and rostral localisation in the CNS. We first generated HB9-Cre⁺ Ai14-tdT^{fl/+} hCD63-GFP^{fl/+} and DAT-Cre⁺ Ai14-tdT^{fl/+} hCD63-GFP^{fl/+} triple positive mice to selectively label spinal cord motor neurons and midbrain dopaminergic neurons, respectively, so that hCD63-GFP⁺ alone signals, presumably extracellular exosomes, and hCD63-GFP⁺tdT⁺ signals, an indication of intracellular ILVs, can be better separated. Spinal cord and midbrain sections from different ages of HB9-Cre⁺ Ai14-tdT^{fl/+} hCD63-GFP^{fl/+} and DAT-Cre⁺ Ai14-tdT^{fl/+} hCD63-GFP^{fl/+} mice were prepared, and representative images were collected respectively with confocal microscopy. Extracellularly localised hCD63-GFP signals outside of tdT⁺ neuronal cell body,

presumably secreted exosomes, were found as early as E12 in the spinal cord of HB9-Cre⁺ Ai14-tdT^{fl/+} hCD63-GFP^{fl/+} mice (white arrows, Figure 6A) and E18 in substantia nigra of DAT-Cre⁺ Ai14-tdT^{fl/+} hCD63-GFP^{fl/+} mice (white arrows, Figure 6B). Quantification of hCD63-GFP⁺ alone and hCD63-GFP⁺tdT⁺ co-localised signals found consistent and substantial secreted exosomes, indicated by 18%–20% hCD63-GFP⁺ alone signals, from HB9⁺ and DAT⁺ neurons across early postnatal developmental stages (Figure 6C).

To further illustrate hCD63-GFP labelling near synapses and blood vessels with increased resolution, we generated AAV-DIO-hSyn-hCD63-GFP virus and performed the stereotaxic injection into the ventral tegmental area (VTA) of adult DAT-Cre⁺ mice (Figure 6D), which helps achieve increased hCD63-GFP signals to facilitate GFP immunogold labelling on midbrain sections. We first injected AAV-DIO-hCD63-GFP into the VTA and confirmed effective and focal induction of hCD63-GFP on DAT-Cre mice (Figure 6D). As hCD63-GFP is only induced from DAT⁺ neurons in DAT-Cre mice, hCD63-GFP⁺ signals and labelled vesicles indicate intracellular ILVs and secreted exosomes from DAT⁺ neurons. In contrast to our previous observations from CaMKII⁺ excitatory neurons in forebrain (Men et al. 2019), hCD63-GFP⁺ immunogold signals were commonly (63 ± 5.6% of all axon terminals examined, Figure 6F) found in pre-synaptic axon terminals (Figure 6Ei and enlarged view in Figure 6Eii, yellow arrows). Interestingly, the hCD63-GFP⁺ vesicle (red arrow, Figure 6Eii) is substantially larger in size (100 nm) than typical synaptic vesicle size (20–30 nm) near the synaptic cleft. Excitingly, we also observed vesicular budding from the plasma membrane of the axon terminal (Figure 6Eiii–iv) with a hCD63-GFP⁺ vesicle (50–100 nm size, red arrow, Figure 6Eiv) outside of the axon terminal near the budding site, supporting the secretion of hCD63-GFP⁺ vesicle from the axonal terminal. Dendritic labelling of hCD63-GFP was also observed (yellow arrows, Figure 6Ev–vi,F). In addition, a hCD63-GFP⁺ vesicle with surface hCD63-GFP labelling (yellow arrows) was also found near the lumen of the blood vessel (Figure 6Evii–viii). Together, these immunoEM results clearly support the widespread presence of secreted EVs from DAT⁺ neurons in the VTA.

4 | Discussion

Our current study examined the cellular regulation of ILV biogenesis by glutamate stimulation in the endosome by following the subcellular trafficking of ILV and exosome surface marker CD63 in neurons. Our co-localisation analysis between hCD63-GFP and early endosome and MVB markers, as well

in ii-e: hM3Dq-mCherry⁺ c-Fos⁺ neurons. Blue arrows in ii-d: hCD63-GFP signals inside mCherry⁺ neurons. (C) The orthogonal view of the single Z-focal plane from the Bii-d. Blue arrows: co-localisation of hCD63-GFP signals with mCherry in the neuron. (D) Quantification of c-Fos intensity from control and hM3Dq⁺ cortical sides of injected mice with or without CNO administration, represented by the percentage change of normalised c-Fos signal intensity relative to the control side. *n* = 3 mice, 3–5 fields/5 brain sections/mouse. *p* values determined from one-way ANOVA. (E) Representative images (10×) from near the injection site (0.0 mm) showing the expression of hCD63-GFP and hM3Dq-mCherry and from the distant section (2.4 mm from the injection site) showing the continuous expression of hCD63-GFP (yellow arrows in ii, with no visible mCherry signals) following CNO administration; Scale bar: 1 mm; Quantification of hCD63-GFP⁺ brain area at different distance from the injection site (0.0, 1.2 and 2.4 mm) from CNO-administered (+CNO, F) and CNO free (–CNO, G) mice. Note the sections were 1.2 and 3 mm from the injection site in –CNO groups. *n* = 3 images/distance/mouse, 6 mice/group (+CNO), 3 mice/group (–CNO); *p* values determine from two-way ANOVA with post-hoc Šidák test.

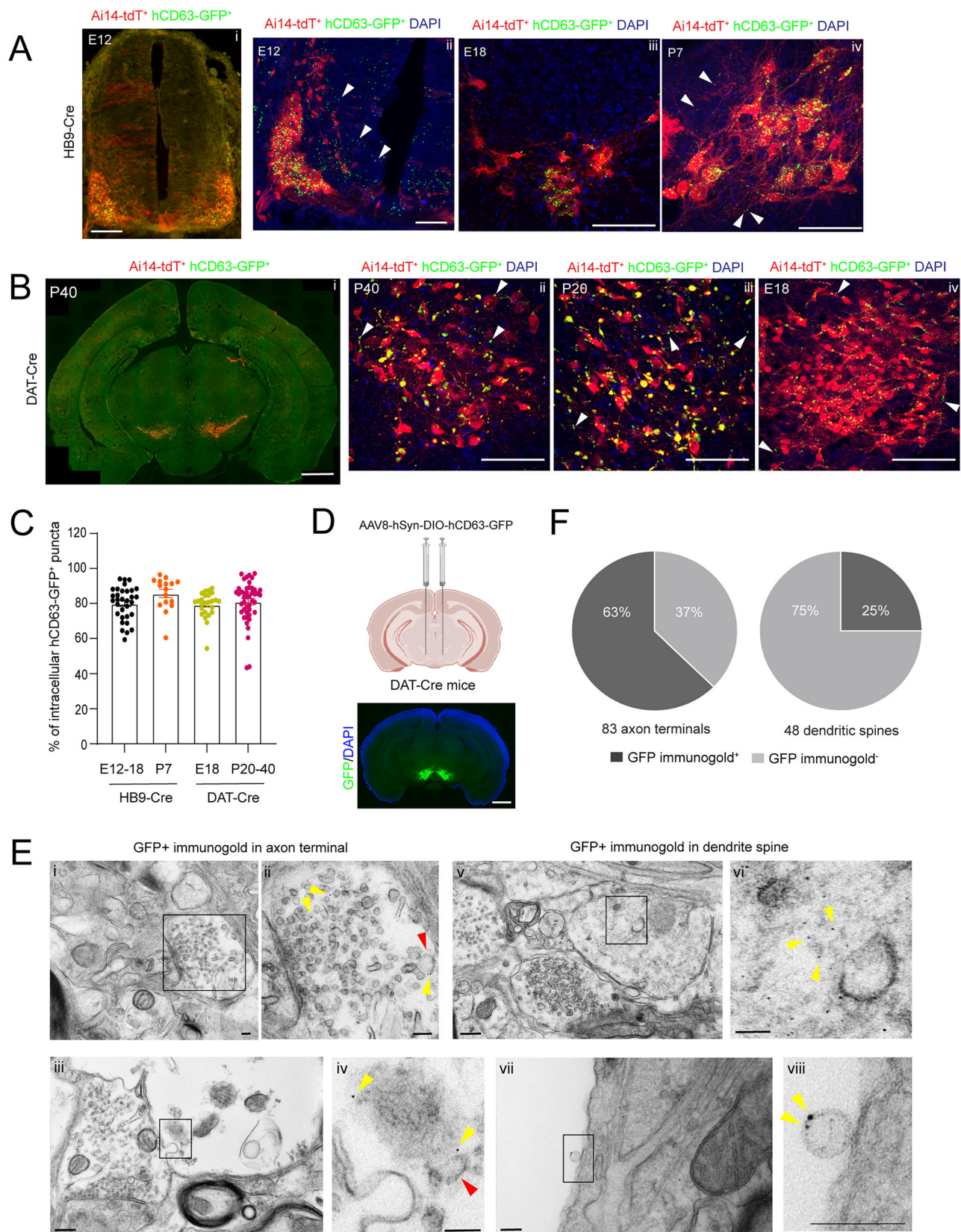


FIGURE 6 | In vivo illustration of intracellular hCD63-GFP⁺ ILVs and extracellular exosomes from specialised neuronal subtypes and regions in the CNS. (A) Representative confocal images of spinal cord sections of HB9-Cre⁺hCD63-GFP^{f/+}/Ai14-tdT^{f/+} mice showing tdT⁺ motor neurons with intracellular (tdT⁺GFP⁺) and extracellular hCD63-GFP signals (tdT⁻GFP⁺, white arrows) at prenatal and early postnatal stages. Scale bar: 200 μ m (i), 50 μ m (ii) and 100 μ m (iii–iv). (B) Representative confocal images of midbrain sections of DAT-Cre⁺hCD63-GFP^{f/+}/Ai14^{f/+} mice showing tdT⁺ dopaminergic neurons and intracellular (tdT⁺GFP⁺) and extracellular hCD63-GFP signals (tdT⁻GFP⁺, white arrows) at prenatal and early postnatal stages. Scale

as immunoEM imaging of cultured neurons, showed that ILVs are primarily localised in MVBs and are actively budded from MVBs in neurons. Together with detection of engineered exosome marker hCD63 (and GFP), as well as endogenous exosome (but not MV) marker mCD63 (Mathieu et al. 2021) but not CD9 on isolated neuronal EVs, our results suggest that MVB-originated exosomes, but unlikely plasma membrane-derived MVs, are the predominant secreted EVs from neurons. In addition, our quantitative measurement of EV numbers demonstrated the direct stimulatory effect of glutamate on EV secretion, likely to be mediated by multiple types of glutamate receptors that all lead to elevated intracellular Ca^{2+} levels. Indeed, previous studies also showed that neuronal EV secretion can be Ca^{2+} -dependent (Olivero et al. 2021). It is noteworthy that our quantitative measurement of EV numbers overcomes previous drawbacks of determining EV quantity based on EV protein marker levels, which may only indicate EV protein changes but may not necessarily be associated with EV quantity. Importantly, with the use of cell-type specific exosome reporter mice, we also showed that DREADD-mediated neuronal excitation significantly increases in vivo spreading of cortical neuronal exosomes. These in vitro and in vivo findings provide important insights about how glutamatergic synaptic transmission may stimulate somatodendritic secretion and spreading of exosomes (and other EVs) in the CNS. As neuronal EVs have been implicated in mediating the spreading of specific disease-associated protein aggregates in neurodegenerative diseases (Howitt and Hill 2016), abnormal neuronal activity—especially hyperexcitability, commonly associated with these neurodegenerative diseases, including AD (Targa Dias Anastacio et al. 2022) and ALS (Xie et al. 2023)—may facilitate spreading of protein aggregates by promoting spreading of neuronal EVs, thus contributing to disease pathology. In addition, our immunogold GFP labelling also frequently revealed axonal terminal localisation and budding of hCD63-GFP⁺ vesicles in dopaminergic neurons, potentially suggesting axon-dependent release of exosomes, which is quite opposite to their preferential somatodendritic localisation in forebrain excitatory neurons (Men et al. 2019). However, given the highly heterogeneous neuronal subtypes and functions, such diverse subcellular localisation of ILVs and release is not unexpected. Additional immunoEM analysis of ILVs/exosomes in situ from specialised neuronal subtypes and regions will provide further anatomical evidence of how exosomes operate in comparison to typical synaptic vesicles.

Neuronal EVs in human CSF and plasma, either from control or neurological disease patients, have been commonly enriched and detected by immunoprecipitation of selective surface proteins (Hill 2019; You et al. 2023), suggesting that neurons constantly secrete EVs. By generating double reporter mice that concurrently and selectively label both specialised neuronal subtypes (HB9⁺ MNs or DAT⁺ dopaminergic neurons) and exosomes, we observed

extracellularly localised exosomes as early as in embryonic stages. Developmentally immature neurons have very primitive and less specialised morphology at embryonic and early postnatal stages. Neuronal axons still undergo pathfinding with mostly irregular spontaneous firing and the neural connectivity has not formed yet to have robust and directional synaptic transmission. Thus, neuronal secretion of exosomes and other EVs may serve as important alternative signals to communicate with various CNS cell types during early CNS development. Consistently, previous in vitro studies have shown that human iPSC-derived neurons secrete EVs to promote neurogenesis and circuit assembly (Sharma et al. 2019). Embryonic neurons also secrete EphB2⁺ EVs to induce growth cone collapse by interacting with ephrinB1, which contributes to repulsive axon guidance (Gong et al. 2016). Developing neurons-derived EVs control dendritic spine development through regulation of HDAC2 signalling (Zhang et al. 2021). In parallel, our small RNA-Seq datasets also showed abundant and diverse miRs in neuronal EVs, some of which are predicted to preferentially bind to cell-type specific mRNAs in different CNS cell types. The roles of such selective intercellular miR-mediated genetic regulation in CNS development will be further investigated in future studies.

Although glutamate stimulation significantly promotes secretion of neuronal EVs, our small RNA-Seq results showed that it has a very modest effect on miR profiles of neuronal EVs. By further examining the cellular and EV abundance of selected top miRs, we showed that certain miRs are differentially enriched in EVs. In particular, although miR-124-3p is 100 times less abundant in neurons than miR-9-5p, its abundance in EVs is close to 50% of miR-9-5p in EVs, resulting in >20 times more enrichment than miR-9-5p. This is consistent with previous observations that various RNA-binding proteins, from hnRNPA2B1 and SYNCRIP to Ago2, may selectively bind certain miRs to carry them into EVs for enrichment (McKenzie et al. 2016; Santangelo et al. 2016; Villarroya-Beltri et al. 2013). On the other hand, other miRs, such as miR-125b-5p, is highly abundant in both neurons and neuronal EVs, suggesting that it may enter EVs by non-selective RNA-binding mechanisms (Xia et al. 2022). As EV miRs may preferentially target on different CNS cell types based on predicted mRNA binding, a better understanding of how RNA-binding proteins mediate miR sorting into ILVs will help elucidate EV miR-targeted neuron to other CNS cell-type communication.

While our current study focuses on the effect of glutamate on miR packaging into EVs, whether other important EV cargoes, such as proteins and lipids, are impacted by glutamate remains little known and will be investigated in future studies. Our current study analysed subcellular localisation of exosome marker hCD63-GFP with still images, which can be limited as a “snapshot” of the hCD63-GFP dynamics. Future live cell imaging

bar: 2 mm (i) and 100 μm (ii–iv). (C) Quantitative analysis of co-localisation between hCD63-GFP and tdT at embryonic and early postnatal stages in spinal cord and midbrain sections from HB9-Cre⁺hCD63-GFP^{fl/+} Ai14-tdT^{fl/+} and DAT-Cre⁺hCD63-GFP^{fl/+} Ai14^{fl/+} mice; $n = 18$ –31 sections, 3–5 images/4 sections/3–4 mice/group. (D) The Diagram of bilateral injections of AAV9-hSyn-DIO-hCD63-GFP virus into the VTA of DAT-Cre⁺ mice. A representative image of selective induction of hCD63-GFP at the VTA from AAV9-hSyn-DIO-hCD63-GFP-injected DAT-Cre⁺ mice. Scale bar: 1 mm. (E) Representative immunoEM images of hCD63-GFP⁺ intracellular signals and vesicles in axonal terminal (i–iv), dendrites (v–vi), blood vessel (vii–viii) from VTA of AAV9-hSyn-DIO-CD63-GFP-injected DAT-Cre mice. Scale bar: 100 nm. (F) Pie charts of the percentage of axons or dendrites with GFP⁺ immunogold particles examined. $n = 83$ axon terminals and 48 dendrite spines respectively from 35 images of two mice.

with endosome-to-lysosome network (ELN) markers and hCD63-GFP may provide more information on how glutamate treatment affects subcellular dynamics of hCD63-GFP. In addition, our confocal image-based analysis may not resolve localisation of individual ILVs, which would require super-resolution imaging in the future. As different types of neurons may respond to different neurotransmitters, our study only unveils the subcellular localisation of hCD63-GFP in glutamatergic stimulation. How it is altered in other neuronal types and by different neurotransmitters, as well as the localisation of hCD63-GFP from different types of neurons in vivo, will need to be investigated in the future.

Author Contributions

Marcela Bertolio: Conceptualization (equal); data curation (lead); formal analysis (lead); investigation (lead); project administration (equal); validation (equal); visualization (equal); writing - original draft (equal); writing - review and editing (equal). **Qiyi Li:** Data curation (equal); formal analysis (equal); investigation (equal); visualization (supporting). **Francesca E. Mowry:** Data curation (equal); formal analysis (equal); investigation (equal); visualization (supporting); Writing - original draft (Supporting). **Kathryn E. Reynolds:** formal analysis (equal); investigation (supporting); visualization (supporting); Writing - original draft (supporting). **Rashed Alananzeh:** Formal analysis (supporting). **Haichao Wei:** Formal analysis (equal); writing - original draft (supporting). **Kyoeun Keum:** Investigation (Supporting). **Rachel Jarvis:** Data curation (equal); formal analysis (equal); investigation (equal); validation (equal); writing - original draft (supporting). **Jiaqian Wu:** Project administration (equal); resources (equal). **Yongjie Yang:** Conceptualization (lead); data curation (equal); funding acquisition (lead); project administration (lead); supervision (lead); visualization (lead); writing - original draft (lead); writing - review and editing (lead).

Acknowledgements

Imaging was performed with the assistance of the Tufts Center for Neuroscience Research. EM was performed with the assistance of the Harvard Medical School EM Core Facility. Small RNA library preparation and sequencing were carried out with the assistance of Tufts University Core Facility Genomics Core (supported by NIH shared instrumentation grant 1S10OD032203-01). This work was supported by NIH grants R01NS118747, R01NS125490 and R01AG078728 (Y.Y.).

Conflicts of Interest

The authors declare no conflicts of interest.

Data Availability Statement

Data available on request from the authors.

References

Antoniou, A., L. Auderset, L. Kaurani, et al. 2023. "Neuronal Extracellular Vesicles and Associated microRNAs Induce Circuit Connectivity Downstream BDNF." *Cell Reports* 42: 112063.

Blanchette, C. R., and A. A. Rodal. 2020. "Mechanisms for Biogenesis and Release of Neuronal Extracellular Vesicles." *Current Opinion in Neurobiology* 63: 104–110.

Budnik, V., C. Ruiz-Canada, and F. Wendler. 2016. "Extracellular Vesicles Round off Communication in the Nervous System." *Nature Reviews. Neuroscience* 17: 160–172.

Delpech, J. C., S. Herron, M. B. Botros, and T. Ikezu. 2019. "Neuroimmune Crosstalk Through Extracellular Vesicles in Health and Disease." *Trends in Neuroscience (Tins)* 42: 361–372.

Faure, J., G. Lachenal, M. Court, et al. 2006. "Exosomes Are Released by Cultured Cortical Neurons." *Molecular and Cellular Neuroscience* 31: 642–648.

Gong, J., R. Korner, L. Gaitanos, and R. Klein. 2016. "Exosomes Mediate Cell Contact-Independent Ephrin-Eph Signaling During Axon Guidance." *Journal of Cell Biology* 214: 35–44.

Ha, J. S., C. S. Lee, J. S. Maeng, K. S. Kwon, and S. S. Park. 2009. "Chronic Glutamate Toxicity in Mouse Cortical Neuron Culture." *Brain Research* 1273: 138–143.

Herman, M. A., and C. E. Jahr. 2007. "Extracellular Glutamate Concentration in Hippocampal Slice." *Journal of Neuroscience* 27: 9736–9741.

Hill, A. F. 2019. "Extracellular Vesicles and Neurodegenerative Diseases." *Journal of Neuroscience* 39: 9269–9273.

Howitt, J., and A. F. Hill. 2016. "Exosomes in the Pathology of Neurodegenerative Diseases." *Journal of Biological Chemistry* 291: 26589–26597.

Iguchi, Y., L. Eid, M. Parent, et al. 2016. "Exosome Secretion Is a Key Pathway for Clearance of Pathological TDP-43." *Brain* 139: 3187–3201.

Kim, G., X. Chen, and Y. Yang. 2022. "Pathogenic Extracellular Vesicle (EV) Signaling in Amyotrophic Lateral Sclerosis (ALS)." *Neurotherapeutics* 19: 1119–1132.

Koles, K., J. Nunnari, C. Korkut, et al. 2012. "Mechanism of Evenness Interrupted (Evi)-Exosome Release at Synaptic Boutons." *The Journal of Biological Chemistry* 287: 16820–16834.

Kowal, J., G. Arras, M. Colombo, et al. 2016. "Proteomic Comparison Defines Novel Markers to Characterize Heterogeneous Populations of Extracellular Vesicle Subtypes." *Proceedings of the National Academy of Sciences of the United States of America* 113: E968–977.

Lachenal, G., K. Pernet-Gallay, M. Chivet, et al. 2011. "Release of Exosomes From Differentiated Neurons and Its Regulation by Synaptic Glutamatergic Activity." *Molecular and Cellular Neuroscience* 46: 409–418.

Mathieu, M., N. Nevo, M. Jouve, et al. 2021. "Specificities of Exosome versus Small Ectosome Secretion Revealed by Live Intracellular Tracking of CD63 and CD9." *Nature Communications* 12: 4389.

McKenzie, A. J., D. Hoshino, N. H. Hong, et al. 2016. "KRAS-MEK Signaling Controls Ago2 Sorting Into Exosomes." *Cell Reports* 15: 978–987.

Men, Y., J. Yelick, S. Jin, et al. 2019. "Exosome Reporter Mice Reveal the Involvement of Exosomes in Mediating Neuron to Astroglia Communication in the CNS." *Nature Communications* 10: 4136.

Morel, L., M. S. R. Chiang, H. Higashimori, et al. 2017. "Molecular and Functional Properties of Regional Astrocytes in the Adult Brain." *Journal of Neuroscience* 37: 8706–8717.

Morel, L., M. Regan, H. Higashimori, et al. 2013. "Neuronal Exosomal miRNA-Dependent Translational Regulation of Astroglial Glutamate Transporter GLT1." *Journal of Biological Chemistry* 288: 7105–7116.

Olivero, G., F. Cisani, D. Marimipietri, et al. 2021. "The Depolarization-Evoked, Ca(2+)-Dependent Release of Exosomes from Mouse Cortical Nerve Endings: New Insights Into Synaptic Transmission." *Frontiers in Pharmacology* 12: 670158.

Pastuzyn, E. D., C. E. Day, R. B. Kearns, et al. 2018. "The Neuronal Gene Arc Encodes a Repurposed Retrotransposon Gag Protein That Mediates Inter cellular RNA Transfer." *Cell* 173: 275.

Pols, M. S., and J. Klumperman. 2009. "Trafficking and Function of the Tetraspanin CD63." *Experimental Cell Research* 315: 1584–1592.

Razzauti, A., and P. Laurent. 2021. "Ectocytosis Prevents Accumulation of Ciliary Cargo in *C. elegans* Sensory Neurons." *Elife* 10: e67670.

Santangelo, L., G. Giurato, C. Cicchini, et al. 2016. "The RNA-Binding Protein SYNCRIP Is a Component of the Hepatocyte Exosomal Machinery Controlling MicroRNA Sorting." *Cell Reports* 17: 799–808.

Schiapparelli, L. M., P. Sharma, H. Y. He, et al. 2022. "Proteomic Screen Reveals Diverse Protein Transport Between Connected Neurons in the Visual System." *Cell Reports* 38: 110287.

- Segel, M., B. Lash, J. Song, et al. 2021. "Mammalian Retrovirus-Like Protein PEG10 Packages Its Own mRNA and Can be Pseudotyped for mRNA Delivery." *Science* 373: 882–889.
- Sharma, P., P. Mesci, C. Carromeu, et al. 2019. "Exosomes Regulate Neurogenesis and Circuit Assembly." *Proceedings of the National Academy of Sciences of the United States of America* 116: 16086–16094.
- Targa Dias Anastacio, H., N. Matosin, and L. Ooi. 2022. "Neuronal Hyperexcitability in Alzheimer's Disease: What Are the Drivers Behind this Aberrant Phenotype?" *Translational Psychiatry* 12: 257.
- Villarroya-Beltri, C., C. Gutierrez-Vazquez, F. Sanchez-Cabo, et al. 2013. "Sumoylated hnRNP A2B1 Controls the Sorting of miRNAs Into Exosomes Through Binding to Specific Motifs." *Nature Communications* 4: 2980.
- Wan, C., M. H. B. Stowell, and J. Shen. 2022. "Progress and Gaps of Extracellular Vesicle-Mediated Intercellular Cargo Transfer in the central Nervous System." *Communications Biology* 5: 1223.
- Wang, Y., V. Balaji, S. Kaniyappan, et al. 2017. "The Release and Trans-Synaptic Transmission of Tau via Exosomes." *Molecular Neurodegeneration* 12: 5.
- Xia, X., Y. Wang, Y. Qin, S. Zhao, and J. C. Zheng. 2022. "Exosome: A Novel Neurotransmission Modulator or Non-Canonical Neurotransmitter?" *Ageing Research Reviews* 74: 101558.
- Xie, M., P. N. Pallegar, S. Parusel, A. T. Nguyen, and L. J. Wu. 2023. "Regulation of Cortical Hyperexcitability in Amyotrophic Lateral Sclerosis: Focusing on Glial Mechanisms." *Molecular Neurodegeneration* 18: 75.
- Xu, B., Y. Zhang, X. F. Du, et al. 2017. "Neurons Secrete miR-132-Containing Exosomes to Regulate Brain Vascular Integrity." *Cell Research* 27: 882–897.
- You, Y., Z. Zhang, N. Sultana, et al. 2023. "ATP1A3 as a Target for Isolating Neuron-Specific Extracellular Vesicles From human Brain and Biofluids." *Science Advances* 9: eadi3647.
- Zhang, L., T. V. Lin, Q. Yuan, R. Sadoul, T. T. Lam, and A. Bordey. 2021. "Small Extracellular Vesicles Control Dendritic Spine Development Through Regulation of HDAC2 Signaling." *Journal of Neuroscience* 41: 3799–3807.
- Zhang, Y., K. Chen, S. A. Sloan, et al. 2014. "An RNA-Sequencing Transcriptome and Splicing Database of Glia, Neurons, and Vascular Cells of the Cerebral Cortex." *Journal of Neuroscience* 34: 11929–11947.

Supporting Information

Additional supporting information can be found online in the Supporting Information section.